Bioactive Materials 44 (2025) 339–353

Contents lists available at ScienceDirect

Bioactive Materials

journal homepage: www.keaipublishing.com/en/journals/bioactive-materials

Periosteum-bone inspired hierarchical scaffold with endogenous piezoelectricity for neuro-vascularized bone regeneration

Yao Zhao [a,1], Yunfan Cai [a,b,1], Wenkai Wang [a,c], Yongkang Bai [a], Mingyi Liu [a], Yan Wang [a], Wen Niu [a], Zhixiao Luo [b], Lingyun Xia [b], Juanfang Zhu [c], Fei Zhao [a], Franklin R. Tay [d], Lina Niu [a,*]

[a] State Key Laboratory of Oral & Maxillofacial Reconstruction and Regeneration, National Clinical Research Center for Oral Diseases, Shaanxi Key Laboratory of Stomatology, Department of Prosthodontics, School of Stomatology, The Fourth Military Medical University, Xi'an, Shaanxi, 710032, PR China
[b] Department of Stomatology, Taihe Hospital, Hubei University of Medicine, Shiyan, Hubei, 442000, PR China
[c] Department of Stomatology, The First Affiliated Hospital of Zhengzhou University, Zhengzhou, Henan, 450052, PR China
[d] The Dental College of Georgia, Augusta University, Augusta, GA, 30912, USA

ARTICLE INFO

Keywords:
Bone repair
Biomineralization
Piezoelectricity
Neuro-vascularization
Periosteum

ABSTRACT

The development of scaffolds for repairing critical-sized bone defects heavily relies on establishing a neuro-vascularized network for proper penetration of nerves and blood vessels. Despite significant advancements in using artificial bone-like scaffolds infused with various agents, challenges remain. Natural bone tissue consists of a porous bone matrix surrounded by a neuro-vascularized periosteum, with unique piezoelectric properties essential for bone growth. Drawing inspiration from this assembly, we developed a periosteum-bone-mimicking bilayer scaffold with piezoelectric properties for regeneration of critical-sized bone defects. The periosteum-like layer of this scaffold features a double network hydrogel composed of chelated alginate, gelatin methacrylate, and sintered whitlockite nanoparticles, emulating the viscoelastic and piezoelectric properties of the natural periosteum. The bone-like layer is composed of a porous structure of chitosan and bioactive hydroxyapatite created through a biomineralization process. Unlike conventional bone-like scaffolds, this bioinspired bilayer scaffold significantly enhances osteogenesis, angiogenesis, and neurogenesis combined with low-intensity pulsed ultrasound-assisted piezoelectric stimulation. Such a scheme enhances neuro-vascularized bone regeneration *in vivo*. The results suggest that the bilayer scaffold could serve as an effective self-powered electrical stimulator to expedite bone regeneration under dynamic physical stimulation.

1. Introduction

The repair of critical-sized bone defects caused by trauma and various bone diseases presents a significant clinical challenge and poses a serious threat to patient health [1]. It is well recognized that bone growth is tightly linked to the regulation of nerves and blood vessels [2,3]. Sensory nerves are crucial for maintaining bone homeostasis. These nerves support bone regeneration by monitoring bone density and metabolism [4–6]. In addition, blood vessels are essential for transporting nutrients and facilitating cellular exchanges necessary for cell growth [7,8]. Notably, vascularization enhances the early expression of neuropeptide receptors, providing an environment conducive to nerve regeneration, thereby accelerating bone defect repair [9,10]. Notable advancements have been made in tissue-engineered scaffolds by incorporating a variety of functional active agents. Nevertheless, challenges such as inadequate osteogenesis and adverse effects like biotoxicity and ectopic ossification limit their clinical use [11–13]. Therefore, developing functional scaffolds that can rapidly induce neuro-vascularization without relying on active agents is critical for enhancing bone defect repair [14]. Such an endeavor represents a major focus and challenge in contemporary bone tissue engineering research.

Natural bone tissue has a hierarchical structure. This structure includes a rigid bone matrix and a flexible periosteum [15,16]. The bone matrix is a three-dimensional (3D) porous structure made of mineralized

Peer review under responsibility of KeAi Communications Co., Ltd.
* Corresponding author. The Fourth Military Medical University, Xi'an, Shaanxi, PR China.
E-mail address: niulina831013@126.com (L. Niu).
[1] These authors contributed equally to this work.

https://doi.org/10.1016/j.bioactmat.2024.10.020
Received 9 July 2024; Received in revised form 19 October 2024; Accepted 19 October 2024

collagen [17]. The periosteum covers the bone surface. It acts as a flexible piezoelectric material, mainly composing of collagen fibrils. These fibrils have a polar hexagonal crystalline unit and a spiral structure [18–20]. The periosteum is rich in a neuro-vascularized network. This network supplies essential nutrients and growth factors for bone growth. The network also affects cell fate and osteogenesis through its electrophysiological effects [21,22]. When bone defects occur, damage to the periosteum is inevitable [23]. To date, tissue-engineered scaffolds only mimic the mineralized bone matrix. These scaffolds have not considered the critical role of the periosteum in bone healing [24]. Research shows that the periosteum contributes over 70 % to early osteogenesis during fracture repair. Damage to the periosteum can slow or even stop bone repair [25,26]. Thus, there is an urgent need for a new artificial bone implant. This implant should mimic both the structure and function of natural bone tissue, including both the periosteum and the mineralized bone matrix.

Electrical stimulation has been clinically proven to promote bone regeneration [27,28]. However, external electrical stimulation is invasive and increases infection risk [29]. Piezoelectric materials can generate electrical stimulation instantly in response to mechanical stresses [30–32]. Low-intensity pulsed ultrasound (LIPUS) is approved by the US Food and Drug Administration because of its deep tissue penetration potential and safety [33,34]. These bioelectrical signals are crucial for nerve transmission, communication between cells, cell division, and ion transport [20,35,36]. Although piezopolymers (e.g., polyvinylidene fluoride) and piezoceramics (e.g. zirconate titanate, zinc oxide) facilitate tissue regeneration, their non-biodegradable and toxic nature impose unresolvable challenges for biological use [37–39]. There is a pressing need for bone scaffolds that incorporate bioactive piezoelectric materials to recreate the electrophysiological environment for expedited bone regeneration. Whitlockite (WH) nanoparticles, the second most abundant inorganic bone mineral, contain magnesium-infused calcium phosphate ($Ca_9Mg(HPO_4)(PO_4)_6$) [40]. Sintered WH exhibits bioactivity akin to carbonated apatite found in natural bone, and possesses unique piezoelectric properties [41]. Hence, there is potential for sintered WH to be used in bone tissue engineering.

A periosteum-bone biomimetic piezoelectric scaffold was developed in the present work that was inspired by the heterostructure and unique function of natural bone tissue. This scaffold has a mineralized bone-like layer and a periosteum-like layer. Rigid bone matrix Bone, as a mineralized tissue, consists primarily of collagen molecules and hydroxyapatite, the latter exhibiting remarkable osteoinductive properties. To replicate the composition and process of bone mineralization, chitosan—a biocompatible biomaterial abundant in amino groups—was utilized as a mineralization template. This facilitates the *in-situ* growth of hydroxyapatite nanoparticles, resulting in the formation of a chitosan-hydroxyapatite (CS/HAp) 3D bone-like layer. The periosteum-like layer on top of the bone-like layer simulates the embedding pattern of Sharpey's fibers. It consists of a flexible double network hydrogel made from calcium-chelated biocompatible alginate and covalently cross-linked gelatin methacryloyl (GM/Alg). Piezoelectric WH (PWH) nanoparticles were incorporated within the periosteum-like hydrogel to bestow the hydrogel with piezoelectric properties. The result is an innovative scaffold with a bilayer structure and inherent piezoelectricity (Scheme 1). When subjected to LIPUS stimulation, this bioinspired scaffold with piezoelectricity significantly improves early vascularization and neurogenesis. This facilitates bone repair by reconstructing bone defect architecture and modulating the bioelectric microenvironment. To the authors knowledge, this periosteum-bone mimicking scaffold has not yet been reported. The bioinspired piezoelectric scaffold represents a convenient and effective method for neuro-vascularized bone regeneration.

2. Materials and methods

2.1. Materials

Calcium hydroxide ($Ca(OH)_2$), magnesium hydroxide ($Mg(OH)_2$), calcium chloride ($CaCl_2$), sodium hydroxide (NaOH), sodium dihydngen phoshate anhydrous (NaH_2PO_4), phosphoric acid, and chitosan (CS, 90 % deacetylated) were purchased from Aladdin (Shanghai, China). Methacrylic anhydride, lithium phenyl (2,4,6-trimethylbenzoyl) phosphinate (LAP), and FITC-labeled phalloidin were obtained from Millipore Sigma, (Burlington, MA, USA). Type A gelatin was purchased from Maokang (Guangzhou, China). Sodium alginate (Alg), Triton X-100, bovine serum albumin, and calcein-AM/PI double staining kit were purchased from Solarbio (Beijing, China). Prime Script RT reagent kit and Trizol RNA extract kit were obtained from Takara (Shiga, Japan). All of the chemicals were of analytical grade.

2.2. Synthesis of piezoelectric whitlockite (PWH) nanoparticles

Whitlockite nanoparticles were synthesized using the precipitation technique [42]. Briefly, $Ca(OH)_2$ (0.37 M) and $Mg(OH)_2$ (0.13 M) were

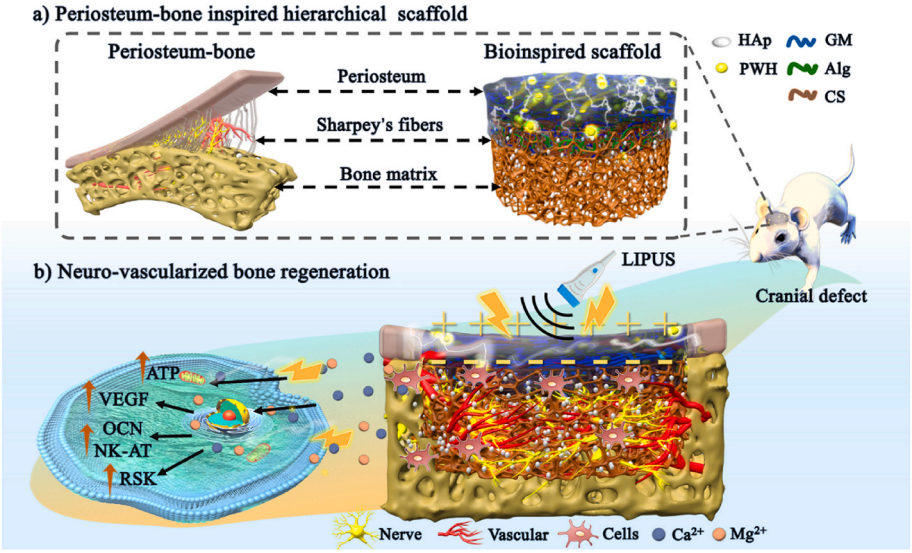

Scheme 1. Schematic of a bioinspired scaffold with endogenous piezoelectricity for bone defect repair. a) The design of periosteum-bone inspired hierarchical scaffold. b) The bioinspired scaffold with endogenous piezoelectricity and bioactive components for neuro-vascularized bone regeneration.

mixed with deionized water and maintained at 100 °C for 30 min. This was followed by dropwise addition of phosphoric acid (0.5 M) at a rate of 0.5 mL/s. The reaction was heated at 100 °C for 10 h (pH 5). After aging at room temperature, the milky white precipitates were centrifuged (6000 rpm, 15 min), washed, and dried overnight at 80 °C to produce WH nanoparticles. To induce the piezoelectricity, the prepared WH powder was subjected to a heating process in a muffle furnace. The temperature was ramped up at a rate of 10 °C/min to reach 650 °C, where it was held isothermally for 3 h. Following this, the material was allowed to cool naturally overnight. This process resulted in the synthesis of PWH nanoparticles with piezoelectric effects.

2.3. Fabrication of the bilayer scaffold (Bio-S)

This scaffold featured a bilayer structure similar to relationship between bone and periosteum. The lower layer, made of chitosan and hydroxyapatite (CS/HAp), functions as the bone-like scaffold and was referred to as the B-S layer. The upper layer, composed of a gelatin methacryloyl, alginate, and PWH hydrogel (GM/Alg/PWH hydrogel), functions as the periosteum-like scaffold and was referred to as the P-S layer.

Synthesis of CS/HAp scaffold: Chitosan (CS) was dissolved in acetic acid (2 %, w/v) through magnetic stirring to achieve complete dissolution. Subsequently, $CaCl_2$ (2 mol/L) and NaH_2PO_4 (1.2 mol/L) were added and stirred for 1 h. The mixture was freeze-dried. The dried material was immersed in a NaOH (1.25 wt%, pH = 13) for 8 h. This was followed by washing with deionized water until neutralization was achieved to produce the CS/HAp scaffold.

Synthesis of GM/Alg/PWH hydrogel: Gelatin methacryloyl (GM) was synthesized by dissolving 5 g of type A gelatin in 50 mL of deionized water. Subsequently, 12.5 mL of methacrylic anhydride was added, and the mixture was continuously stirred at 55 °C for 2 h. The solution was dialyzed (molecular weight cut-off 8000–14000 Da) for 7 days to remove unreacted methacrylic acid. The resulting GM foam was obtained through a 3-day freeze-drying process. The GM foam (10 %, w/v) and alginate (Alg, 20 %, w/v) were dissolved in phosphate-buffered saline (PBS) at 55 °C until completely dissolved. PWH nanoparticles (15 % wt) were then added to the solution and stirred for 1 h. Subsequently, 0.25 % (w/v) lithium phenyl (2,4,6-trimethylbenzoyl) phosphinate (LAP) was dripped into the solution to obtain the precursor fluid of the P-S hydrogel. The precursor solution was cured with ultraviolet light for 5 min and then immersed in a $CaCl_2$ solution for 10 min. The GM/Alg/PWH hydrogel was obtained after rinsing 3 times with deionized water.

Fabrication of the bilayer scaffold: Uncured precursor solution of the GM/Alg/PWH hydrogel was poured onto the B-S layer. The bilayer scaffold developed in this work is cylindrical, with an upper-to-lower layer thickness ratio of 1:2. It was allowed to penertrate naturally for a 3 min before polymerization with ultraviolet irradiation for 5 min. The hydrogel layer was then suspended in a $CaCl_2$ solution for another 10 min to generate the Bio-S scaffold.

2.4. Physicochemical characterization of the bilayer scaffold

Scanning electron microscopy (SEM) images and element mapping were obtained using a FEU 430 NanoSEM (Lausanne, Switzerland) at an acceleration voltage of 15 kV. The composition and crystalline structure of each specimen was analyzed by Fourier transform infrared spectroscopy (FTIR, FTIR-8400S, Shimadzu, Kyoto, Japan) and X-ray diffraction (XRD, Bruker D8 Advance, Billerica, MA, USA).

2.5. Piezoelectric coefficient measurement

Piezoelectric whitlockite nanoparticles were compacted into discs measuring 10 mm in diameter and 2 mm in thickness. For piezoelectric measurements, the upper and lower surfaces of the discs were coated with silver paste as a conductive agent. Polarization was achieved by applying a direct current electric field of 5 kV/cm to the discs at room temperature for 30 min. The piezoelectric coefficients of the PWH disc were measured using a quasi-static d33 m device (ZJ-3AN, IACAS, China). The piezoelectric coefficients of GM/Alg/WH and GM/Alg/PWH hydrogels (diameter: 10 mm, height: 2 mm) were also determined [43].

2.6. Piezoelectric performance test

A programmable electrometer (KEITHLEY6514, Keithley, USA) was used to detect the piezoelectric performance of the hydrogels. For the GM/Alg/WH and GM/Alg/PWH hydrogels, square slices were prepared and single-sided silver conductive tape was affixed to the top and bottom surfaces. Two copper wires were then drawn from each end of the tape. An insulating polyurethane film was then used to encapsulate the hydrogels. To evaluate the piezoelectric response, the hydrogel surface was subjected to cyclic forces of 0.25 N, 0.5 N, 1 N, and 2 N at a frequency of 1 Hz. The resulting changes in voltage were recorded using the electrometer. To visualize the piezoelectricity of the hydrogel, copper wires were employed to connect both sides of the GM/Alg/WH and GM/Alg/PWH hydrogels encapsulated with PU insulator membranes in a circuit. This circuit contained a small LED bulb that was connected in series with signal amplifiers.

2.7. Rheology measurements of the hydrogel

The rheological properties of the hydrogels were measured using a rotary rheometer (DHR-2, TA Instruments, New Castle, DE, USA). A shear-thinning test was performed with a shear rate ranging from 0 to 100 s^{-1}. The frequency was maintained at 10 rad/s under 1 % strain. The strain amplitude was varied with the frequency held constant at 10 rad/s, ranging from 1 to 100 %. A step-strain sweep test was conducted with alternating low strain ($\gamma = 5$ %) to high strain ($\gamma = 300$ %) at a constant frequency of 10 rad/s to examine the recovery behavior of the GM/Alg/PWH hydrogel.

2.8. Mechanical properties of the bilayer scaffold

The compressive properties of the scaffolds were evaluated using a universal mechanical force testing machine (AGS-10KN, Japan). Samples (B-S, P-S, and Bio-S) with dimensions of $\Phi 10 \times 4$ mm were tested at a cross-head speed of 1.0 mm/min. Compressive stress was recorded with a deformation of 70 %. Three parallel samples were tested to ensure consistency in the measurements.

2.9. In vitro degradation of the bilayer scaffold

The degradation behavior of the B-S and P-S components of the bilayer scaffold was investigated by immersing the specimens in phosphate-buffered saline (PBS) containing lysozyme and collagenase (0.5 mg/mL) in a shaking bath at 37 °C. The solution was refreshed every two days to maintain the degradation environment. At predetermined time intervals (days 0, 3, 7, 14, 21, 28, and 35), the specimens were removed, cleaned to remove residual PBS, lyophilized, and weighed. The weight loss ratio was detected by the equation.

$$\text{Weight loss ratio (\%)} = (W_2 - W_1) / W_2 \times 100$$

where W_1 and W_2 represent the initial and final weights of the specimens, respectively.

2.10. Ion release behavior of the bilayer scaffold

The Bio-S scaffolds were immersed in PBS (pH = 7.4) at 37 °C. At predetermined intervals (6 h, 12 h, 1 d, 2 d, 4 d, 7 d), the collected liquid was analyzed with inductively coupled plasma-mass spectrometry (ICP-

MS, NexION 2000, PerkinElmer, Waltham, MA, USA) to measure the concentration of Mg^{2+}. Three parallel measurements were conducted for each specimen at each time-point.

2.11. Cytocompatibility of the bilayer scaffold

Murine bone marrow mesenchymal stem cells (BMSCs) were used to examine the cytocompatibility of the scaffolds. The BMSCs were isolated from one-week-old Sprague Dawley rats and cultured in Dulbecco's Modified Eagle Medium (DMEM). The culture medium was supplemented with 100 U/mL penicillin, 0.1 mg/mL streptomycin, and 10 % fetal bovine serum (Bosco Biotechnology Co., Ltd, Shanghai, China). The cells were then incubated in a CO_2 incubator (MCO-15AC, Sanyo, Osaka, Japan) at 37 °C. To simulate piezoelectric stimulation of the BMSCs by the scaffold, a Low-Intensity Pulsed Ultrasound (LIPUS) device was utilized in a cell culture system (WELLD, WED-100, Shenzhen, China). Each scaffold was placed on the LIPUS operating platform. The BMSCs were cultured on the surface of the materials and treated with LIPUS (1 MHz, 0.15 W/cm^2, 20 % pulsed ratio 1:4) [43]. The proliferation of BMSCs co-cultured with different scaffolds was evaluated using the Cell Counting Kit-8 (CCK-8) assay. The BMSCs were seeded onto scaffolds in 96-well plates at a density of 5000 cells/well. The experiment consisted of four groups: Control group (without material), LIPUS, B-S group, B-S + LIPUS group, Bio-S group, and Bio-S + LIPUS group (Bio-S stimulated with LIPUS). LIPUS stimulation was performed daily in the Bio-S + LIPUS group for 10 min each time. After 2 and 4 days, dead (red) and live (green) cells were stained with fluorescein diacetate and propidium iodide and observed using a fluorescence inverted microscope (CLSM, Fluoview FV1000, Japan). In addition, the nucleus and F-actin of the BMSCs were stained in green and blue using DAPI and FITC-labeled phalloidin, respectively.

2.12. In vitro osteogenesis, angiogenesis, and neurogenesis induced by Bio-S + LIPUS

2.12.1. Alkaline phosphatase and alizarin red staining

The BMSCs were seeded onto scaffolds (height: 0.8 mm) in 6-well plates at a density of 3×10^4 cells/well. Osteogenic induction medium (DMEM with 10 % FBS, 1 % penicillin/streptomycin, 50 μM/mL ascorbic acid, 0.1 μM dexamethasone, and 10 mM β-glycerophosphate) was added to replace the medium in the wells. At days 7 and 14, the specimens were retrieved and treated with 4 % paraformaldehyde. Alkaline phosphatase (ALP) staining was performed using a reagent kit according to the manufacturer's specifications to visualize ALP activity. Alizarin red S staining was employed to visualize the deposition of calcified nodules at days 14 and 21.

2.12.2. Reverse transcription-quantitative polymerase chain reaction (RT-qPCR)

The BMSCs were seeded onto scaffolds in 6-well plates at a density of 5×10^4 cells/well. After osteogenic culture for 7 and 14 days, total RNA was extracted from the BMSCs using Trizol reagent and reverse transcribed into cDNA. The cDNA was then subjected to RT-qPCR. Three osteogenesis-related genes: runt-related transcription factor 2 (Runx2), type I collagen (COL I), and osteocalcin (OCN), as well as two angiogenesis-related genes: angiopoietin-1 (Ang-1) and vascular endothelial growth factor (VEGF), were evaluated. Glyceraldehyde 3-phosphate dehydrogenase (GAPDH) was used as the housekeeping gene.

For neurodifferentiation studies, the media were replaced with neural induction medium. The latter was prepared by adding 50 ng/mL NGF-β into the proliferation medium. After 14 days of culture, three neurogenic differentiation genes: nestin, neurofilament light chain (NEFL), and tubulin beta 3 class III gene (TUBB3), were evaluated, with GAPDH as the housekeeping gene. The specific primers used are listed in Table S1 for osteogenesis-related genes, and Table S2 for neurogenic differentiation genes (Supporting Information). The results were calculated using the $2^{-\Delta\Delta Ct}$ method. Values larger than 2 or less than 1/2 were considered statistically significant.

2.12.3. Western blot (WB)

Cells were lysed in radioimmunoprecipitation assay lysis buffer containing protease and phosphatase inhibitors. The BMSCs were seeded onto scaffolds in 6-well plates at a density of 5×10^4 cells/well. The total protein concentration was determined using the bicinchoninic acid (BCA) protein assay kit. Following centrifugation at 12,000 g, the supernatant was heated to 100 °C for 5 min. Subsequently, 20 μg of the protein suspension was separated by sodium dodecyl sulfate-polyacrylamide gel electrophoresis (SDS-PAGE), transferred onto polyvinylidene fluoride membranes, and blocked with 5 % bovine serum albumin. The membranes were then incubated overnight at 4 °C with specific primary antibodies. This was followed by incubation with secondary antibodies at 37 °C. Immunoblots were visualized using an enhanced chemiluminescence kit and quantified with ImageJ software (National Institute of Health, Bethesda, MD, USA). Protein expression levels were normalized to GAPDH. Antibodies used in this study included Runx2, COL I, OCN, Ang-1, VEGF, MEK, P-MEK, ERK, P-ERK, AKT, P-AKT, PI3K and P-PI3K (Affinity Biosciences, Cincinnati, OH, USA).

2.13. Mechanism of vascular-neurogenic osteogenesis

2.13.1. Transcriptome sequencing

RNA-sequencing was used to evaluate mRNA profiles in BMSCs. Analysis was conducted on three groups: B-S group, Bio-S group, and Bio-S + LIPUS group. Briefly, BMSCs (5×10^4 cells/well) were cultured in 6-well plates with B-S and Bio-S specimens for 7 days. The Bio-S + LIPUS group was subjected to LIPUS stimulation daily (0.15 W/cm^2, 10 min each time). On the 7th day, the collected cells were washed three times with PBS, and lysed in a 1.5 mL EP tube. The enriched mRNA was fragmented and reverse-transcribed into cDNA with random primers. All cDNA fragments were amplified using Illumina NovaSeq 6000 (Illumina, San Diego, CA, USA) and analyzed by Novogene Biotech Co., Ltd. (Beijing, China). The DESeq2 software was used to identify differentially expressed genes (DEGs) between the B-S group and Bio-S group, as well as the Bio-S + LIPUS group. A corrected P-value of 0.05 and an absolute fold change (FC) of 1 were set as thresholds for significant differential expression. In addition, gene ontology (GO) enrichment analysis and Kyoto Encyclopedia of Genes and Genomes (KEGG) pathway enrichment were conducted. A corrected P-value <0.05 indicated significant enrichment by DEGs.

2.13.2. Detection of key pathway-associated genes in vitro

BMSCs cultured on Bio-S specimens were subjected to daily LIPUS stimulation (0.15 W/cm^2, 10 min each time). After 14 days of culture in osteogenic medium, total RNA from the BMSCs was reverse-transcribed into cDNA. The gene expressions of HIF-1α, P2X7, and RSK (primers listed in Table S3 of the Supporting Information) were quantitatively examined using RT-qPCR.

2.14. Animal model of calvarial bone defects

Animal protocols were approved and conducted following guidelines established by the Institutional Animal Care and Use Committee of the Fourth Military Medical University (IACUC-2023-kq-029). Eight-week-old male Sprague-Dawley rats (~300 g) were procured from the Laboratory Animal Research Center of the Fourth Military Medical University (Xi'an, China). Prior to the surgical procedure, the rats were anesthetized with intraperitoneal injection of pentobarbital sodium.

After a 7-day acclimatization period, general anesthesia was induced with intraperitoneal injection of pentobarbital sodium (2 %, 40 mg/kg). Full-thickness defects with a diameter of 5 mm were created on the middle ridge of the skull using a trephine. Following scaffold

implantation (The thickness of the periosteal layer and osteoid layer is 1 mm, respectively), muscle and skin of the rats were sutured. The rats were administered penicillin at a dose of 400,000 units for 5 days. They remained active and did not exhibit any post-surgery complications. The rats were divided into four groups: control group (without scaffolds), B-S group, Bio-S group, and Bio-S + LIPUS group. The Bio-S + LIPUS group received LIPUS treatment for 20 min every 2 days and lasted for 4 weeks after the operation (1 MHz, 0.15 W/cm^2). After 8 weeks post-surgery, the cranium was harvested from individual rats and fixed in 4 % polyformaldehyde for subsequent measurement.

2.15. Defect reconstruction and bone regeneration

After 8 weeks post-operation, the rats were euthanized at a designated time-point. The calvarium specimens were used to reconstruct 3D models using micro-computed tomography (micro-CT). Coronal and sagittal images were reconstructed to illustrate new bone growth in the calvarium. Bone volume/tissue volume (BV/TV) and bone mineral density (BMD) were assessed for quantitative analysis of new bone growth within the volume of interest. Corresponding slices were stained with hematoxylin and eosin (H&E) and Masson's trichrome staining to visualize tissue morphology and collagen distribution, respectively. Osteogenesis-related proteins and their gene expressions were examined via immunofluorescence staining and RT-qPCR. Markers such as platelet endothelial cell adhesion molecule-1 (CD-31), calcitonin gene-related peptide (CGRP), runt-related transcription factor 2 (Runx2), type I collagen (COL I), vascular endothelial growth factor (VEGF), and tubulin beta 3 class III gene (TUBB3) were analyzed. Primer sequences of the genes used for RT-qPCR analysis are provided in Table S4 of the Supporting Information.

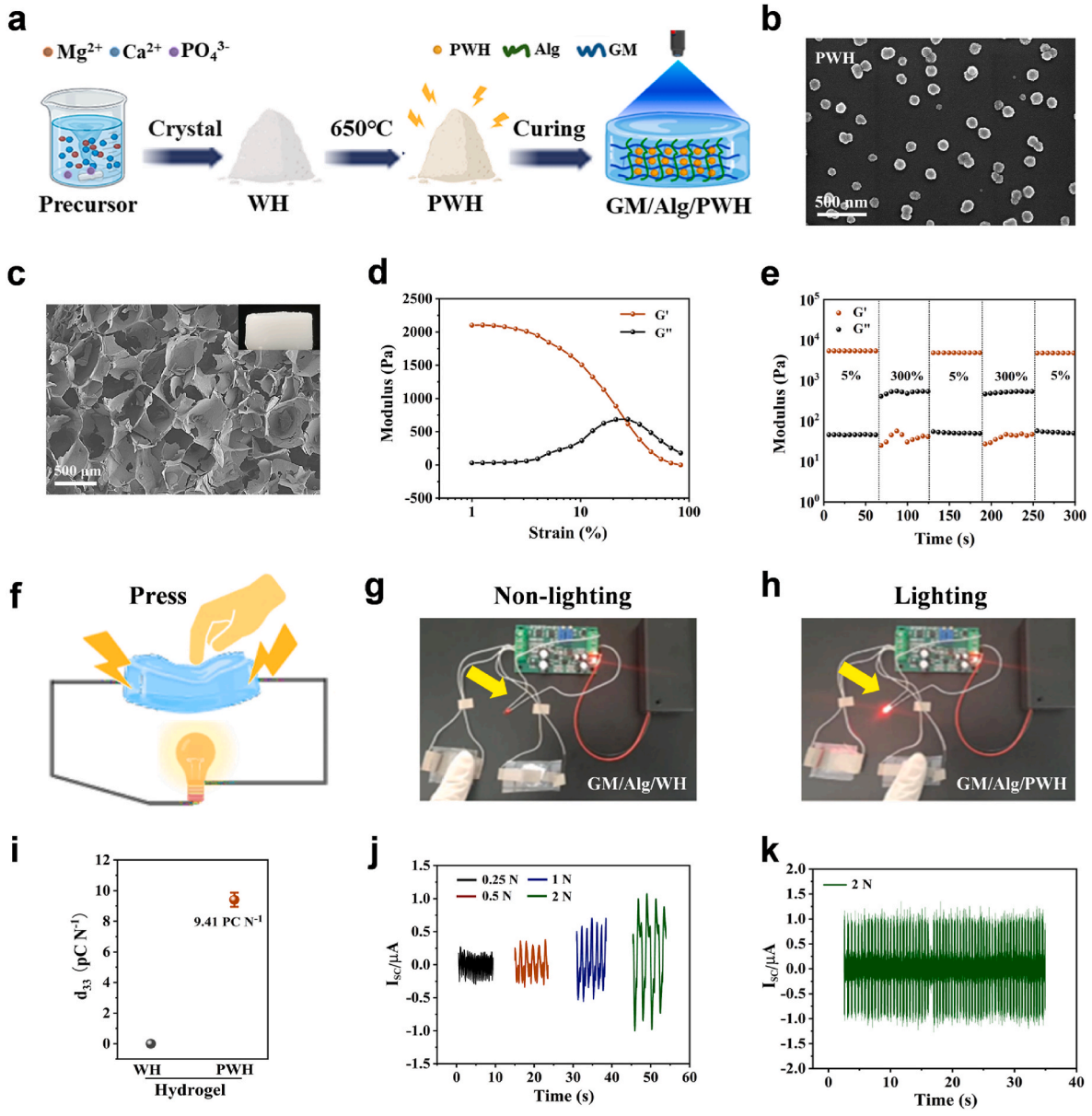

Fig. 1. Characterization of periosteum-like GM/Alg/PWH hydrogel. a) Schematic illustrating the preparation of the GM/Alg/PWH hydrogel. b) Scanning electron microscopy (SEM) image of PWH nanoparticles (bar = 500 μm). c) SEM image of the GM/Alg/PWH hydrogel (bar = 500 nm). Inset shows a photograph of the corresponding hydrogel. d, e) Rheological properties of GM/Alg/PWH hydrogel at 37 °C. f) Schematic and g, h) verification of the GM/Alg/PWH piezoelectric hydrogel in lighting up an LED bulb upon mechanical stimulation. i) Piezoelectric coefficient (d_{33}) of the GM/Alg/WH and GM/Alg/PWH hydrogels. j) Current changes in the GM/Alg/PWH hydrogel system under different force stimulation (frequency: 1 Hz). k) Electrical stability test of the GM/Alg/PWH piezoelectric hydrogel under constant force stimulation (2 N, 1 Hz).

2.16. Statistical analysis

Quantitative data were presented as the mean value ± standard deviation. The differences between two groups were compared using the Student's t-test, and a one-way analysis of variance (ANOVA) followed by Tukey's test was performed to make multiple comparisons. Statistical significance levels were denoted as follows: $*p < 0.05$, $**p < 0.01$, and $***p < 0.001$. Each experiment was conducted with a minimum of three replicates.

3. Results and discussion

3.1. Fabrication and characterization of the periosteum-like piezoelectric hydrogel

To replicate the matrix characteristics and piezoelectricity of the periosteum, WH nanoparticles were first prepared through co-precipitation in an aqueous system (Fig. 1a). The WH nanoparticles were rendered piezoelectric by sintering at 650 °C, resulting in PWH nanoparticles. These PWH nanoparticles were then incorporated into a double network hydrogel made of polymerized gelatin methacryloyl and calcium-chelated alginate (GM/Alg/PWH), creating a periosteum-like piezoelectric hydrogel. Fourier transform infrared spectroscopy (FTIR), X-ray diffraction (XRD) and High-resolution transmission electron microscopy (HRTEM) analyses confirmed the successful fabrication of the GM/Alg/PWH hydrogel scaffold (Fig. S1, S2 and S3). The PWH nanoparticles had a uniform spherical morphology with a diameter of about 100 nm (Fig. 1b). The WH and PWH materials exhibited measurable piezoelectricity with a piezoelectric coefficient of 2.4 pC N^{-1} (Fig. S4). The GM/Alg/PWH hydrogels appeared as white opaque gels. These hydrogels had a 3D porous structure that resembled the fibrous network of the periosteum (Fig. 1c) [44].

The rheological properties of the periosteum-like hydrogel were examined to determine its viscoelastic behavior. Initially, as strain increased, the storage modulus (G′) of the hydrogel exceeded the loss modulus (G″). This phenomenon was indicative of predominantly elastic characteristics [45]. This trend reversed upon reaching ~33 % strain (G' < G″). That is, the hydrogel exhibited viscoelastic behavior, with a broad linear elastic region (Fig. 1d). Moreover, the modulus values of the hydrogel remained stable over time during frequency sweeps, indicating its enhanced structural stability (Fig. S5). Continuous step strain tests showed that at low shear strains of 5 %, G′ was higher than G″. When the shear strain increased to 300 %, both moduli decreased sharply, with G″ becoming higher than G′ due to collapse of the hydrogel. Interesting, when the shear strain was reduced back to 5 % in multiple repetitions, G′ and G″ returned to their initial levels. This feature was indicative of the dynamic recoverability of the hydrogel (Fig. 1e). These findings show that the GM/Alg/PWH hydrogel is viscoelastic with flexibility similar to that of the periosteum [44]. This behavior likely results from the synergistic enhancement mechanism of the double network, formed by the covalent bonds of GM and the chelation of Alg and Ca^{2+} within the hydrogel.

The mechano-electric conversion capability of the GM/Alg/PWH hydrogel was subsequently investigated. Copper wires were used to connect both sides of the GM/Alg/WH and GM/Alg/PWH hydrogels for the demonstration of piezoelectricity. The wires were enclosed in polyurethane insulator membranes and connected to a circuit with a small LED bulb (Fig. 1f). This electrical circuit had no power supply. Pressing on the hydrogel's surface caused the bulb (as shown by the yellow arrow) to light up (Fig. 1g and h). This shows that the PWH nanoparticles rendered the GM/Alg/PWH hydrogel piezoelectric. To further investigate the mechano-electric conversion capability of the GM/Alg/PWH hydrogel, the piezoelectric coefficient of the hydrogel was tested with a value of approximately 9.41 pC N^{-1} (Fig. 1i). This value would be very close to the optimal piezoelectric coefficient value of 10 pC N^{-1} required for bone regeneration [19]. As the applied force increased from 0.25 N to 2 N, the current in the circuit progressively increased (Fig. 1j). This observation indicates that force stimuli can effectively modulate the current magnitude in the hydrogel circuit. When the GM/Alg/PWH hydrogel was stimulated with a constant force of 2 N, a stable electrical signal was also generated in the circuit (Fig. 1k, Fig. S6). This observation indicates that the GM/Alg/PWH hydrogel maintains a stable mechano-electric conversion function. The hydrogel is expected to be reusable many times in the physiologic environment.

3.2. Fabrication and characterization of the periosteum-bone mimicking bilayer scaffold

The chitosan (CS) and hydroxyapatite (HAp) containing bone-mimicking layer was created through freeze-drying technology. During this process, calcium (Ca^{2+}) and phosphate ions (PO_4^{3-}) were regulated *in-situ* regulated by amino groups of CS molecules to induce formation of HAp nanoparticles through a biomineralization process. Subsequently, a mixture of PWH, GM, and Alg was applied onto the bone-mimicking layer and cured by UV irradiation. This yielded a bilayer scaffold reminiscent of the periosteum-bone architecture (Fig. 2a).

The completed scaffold (Bio-S) featured a macroscopic integrated bilayer structure. It consisted of an upper periosteum-like hydrogel scaffold (P-S: GM/Alg/PWH) and a lower mineralized bone-like scaffold (B-S: CS/HAp) (Fig. 2b). Microscopically, both P-S and B-S exhibited a uniform 3D porous structure. The pore size of the P-S layer (~100–350 μm) was larger than that of the B-S layer (~100–200 μm). The sizes of these pores facilitated cell growth, nutrient exchange, and transportation [46]. Prior to ultraviolet light irradiation curing, the upper hydrogel permeated into the lower porous scaffold. This caused the GM and Alg molecules from the upper hydrogel and the lower CS/HAp porous scaffold to form a robust interlocking structure. They created an integrated dense transition interface, similar to cortical bone. This integration resembles how the Sharpey's fibers of the periosteum perforate into cortical bone, establishing a stable connection between the periosteum and the bone matrix [47]. The ingenious preparation method of the bilayer scaffold achieves an exquisite fusion of two-phase heterogeneous structures, which will provide a valuable reference for the design of other multiphase constructions.

At higher magnification, spherical PWH particles, approximately 100 nm in size, were observed on the surface of the P-S pore wall (Fig S7a, Fig. 2b). This distribution matches the previously described morphology of the PWH nanoparticles. The presence of magnesium (Mg) exclusively in the upper layer indicates successful integration of the hydrogel with PWH nanoparticles. Similarly, spindle-shaped inorganic particles, approximately 200 nm in size, were evenly distributed on the surface of the B-S layer (Fig S7b, Fig. 2b). X-ray diffraction confirmed that the particles on the surface of the CS/HAp were HAp (JCPDF#09–0432). The 2θ values of 25.88°, 32.20°, 39.82°, and 46.71° correspond to the (002), (112), (310), and (222) crystallographic planes of HAp, respectively (Fig. 2c). The peaks at 633 cm^{-1}, 605 cm^{-1} and 560 cm^{-1} primarily arise from vibration of the O-P-O bond in the PO_4^{3-} functional group of HAp (Fig. 2d).

Mechanical property testing showed that each group of scaffolds underwent some elastic deformation at the start of compression. As the strain quickly increased, their mechanical strength significantly improved (Fig. S8). Compared to B-S (stress: 0.64 MPa; modulus: 0.47 MPa) and P-S (stress: 0.48 MPa; modulus: 0.46 MPa), the compressive strength of Bio-S was enhanced to 0.77 MPa (Fig. 2e). This enhancement may be attributed to the formation of a robust interlocking structure and an integrated transition interface between the upper and lower layers. Furthermore, the compressive modulus of Bio-S (1.02 MPa) was at least 1.6 times greater than that of B-S and P-S (Fig. 2f). These improved mechanical properties create a relatively stable biomechanical microenvironment that supports cellular growth *in vivo* [48].

Magnesium ions are vital trace element in the human body. These

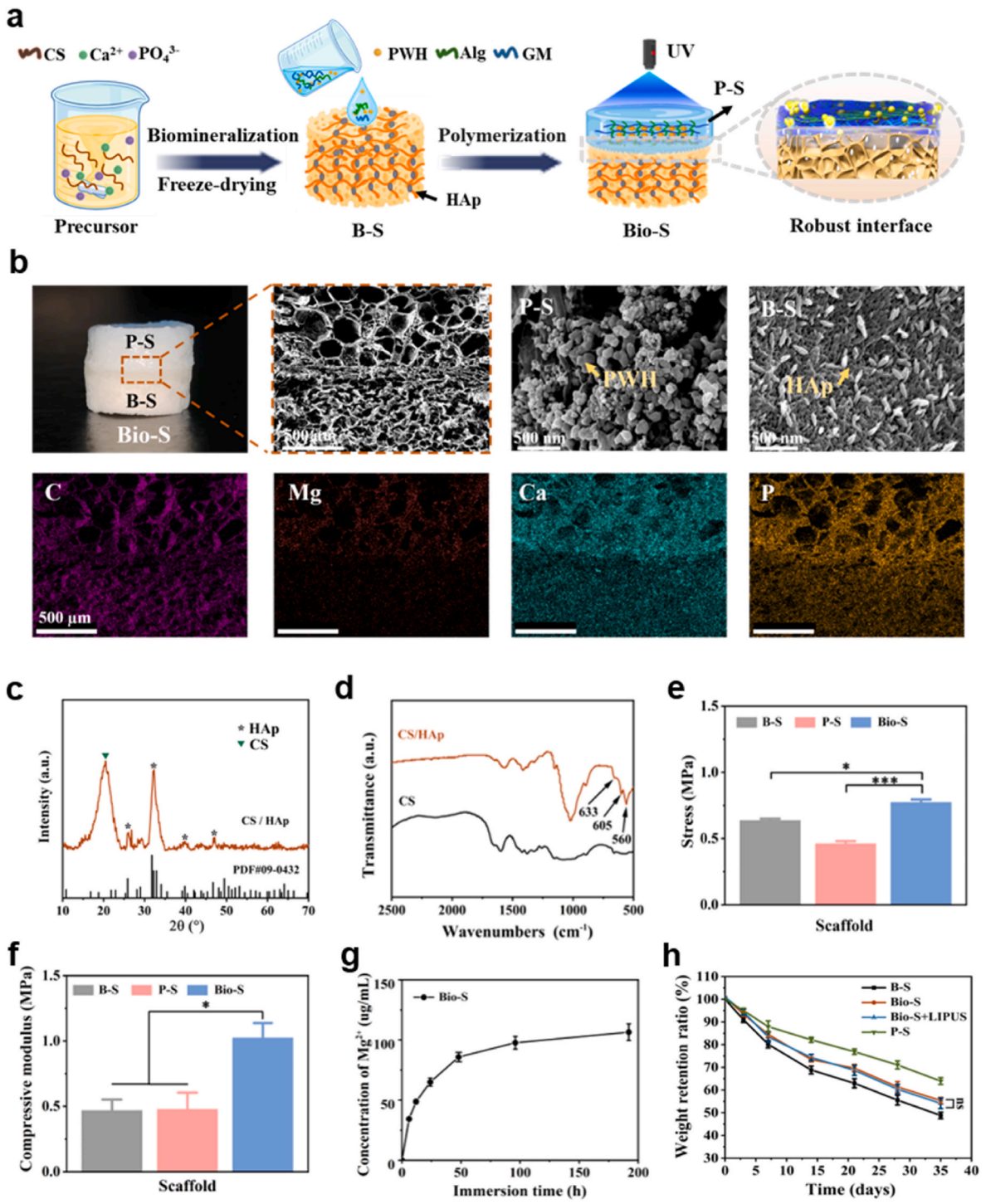

Fig. 2. Characterizations of periosteum-bone bilayer scaffold (Bio-S). a) Schematic of the fabrication process of the bilayer scaffold. b) Fractured cross-section SEM images of the Bio-S and corresponding element mappings (Bars = 500 μm, 500 nm). c) XRD and d) FTIR spectrum of CS/HAp. e) Compressive stress and f) modulus of the B-S, P-S and Bio-S. g) Curve of Mg^{2+} release from the Bio-S over time. h) Degradation of B-S and P-S was tracked in vitro after immersion in phosphate-buffered saline with enzyme at the predetermined time intervals. Data represent means ± standard deviations (n = 5). $^{*}P < 0.05$, $^{***}P < 0.001$. ns denotes no significance.

ions regulate cell behavior enhance cell adhesion, and promote cell differentiation. In addition, they stimulate local bone healing by facilitating angiogenesis [49]. Because Bio-S contains Mg^{2+}-doped PWH nanoparticles, the release behavior of Mg^{2+} from Bio-S was investigated (Fig. 2g). The release of Mg^{2+} from Bio-S exhibited a time-dependent sustained-release pattern. This ensures long-term efficacy in promoting angiogenesis during bone regeneration, and guarantees its local biosafety *in vivo* [50]. Bio-S (PWH) stimulated with LIPUS caused the bulb (as shown by the yellow arrow) to light up (Fig. S9). This suggests that force stimuli generated under LIPUS stimulation can cause Bio-S to generate electrical signals. Being implants *in vivo*, both B-S and P-S exhibited a time-dependent degradation pattern (Fig. 2h). Throughout the testing period, the degradation rate of B-S was consistently higher than that of P-S. For example, by day 35, the degradation ratio of P-S was 35 %, while that of B-S was 45 %. This discrepancy may be attributed to the synergistic anti-enzymatic hydrolysis effect in P-S. This effect is

facilitated by the incorporation of inorganic PWH nanoparticles, and the reinforcement of the double-network structure formed by GM and Alg. The prepared Bio-S scaffold with a degradation ratio between that of B-S and P-S, reaching approximately 46 % by day 35, and no significant differences in degradation ratios were observed between the ultrasound-treated and non-ultrasound-treated groups. Further, the piezoelectric capability of the material after different degradation times was also studied (Fig. S10), our findings indicate that the material exhibits degradation over time, leading to a slightly reduction in the current intensity generated under specific mechanical stimulation. The reduction in piezoelectric intensity after 28 days was minimal compared to the initial state. This suggests that Bio-S can ensure a prolonged piezoelectric effect as bone heals over an extended period.

3.3. Osteogenesis, angiogenesis, and neurogenesis of the bilayer scaffold upon LIPUS stimulation in vitro

The impact of noninvasive LIPUS-assisted piezoelectric stimulation

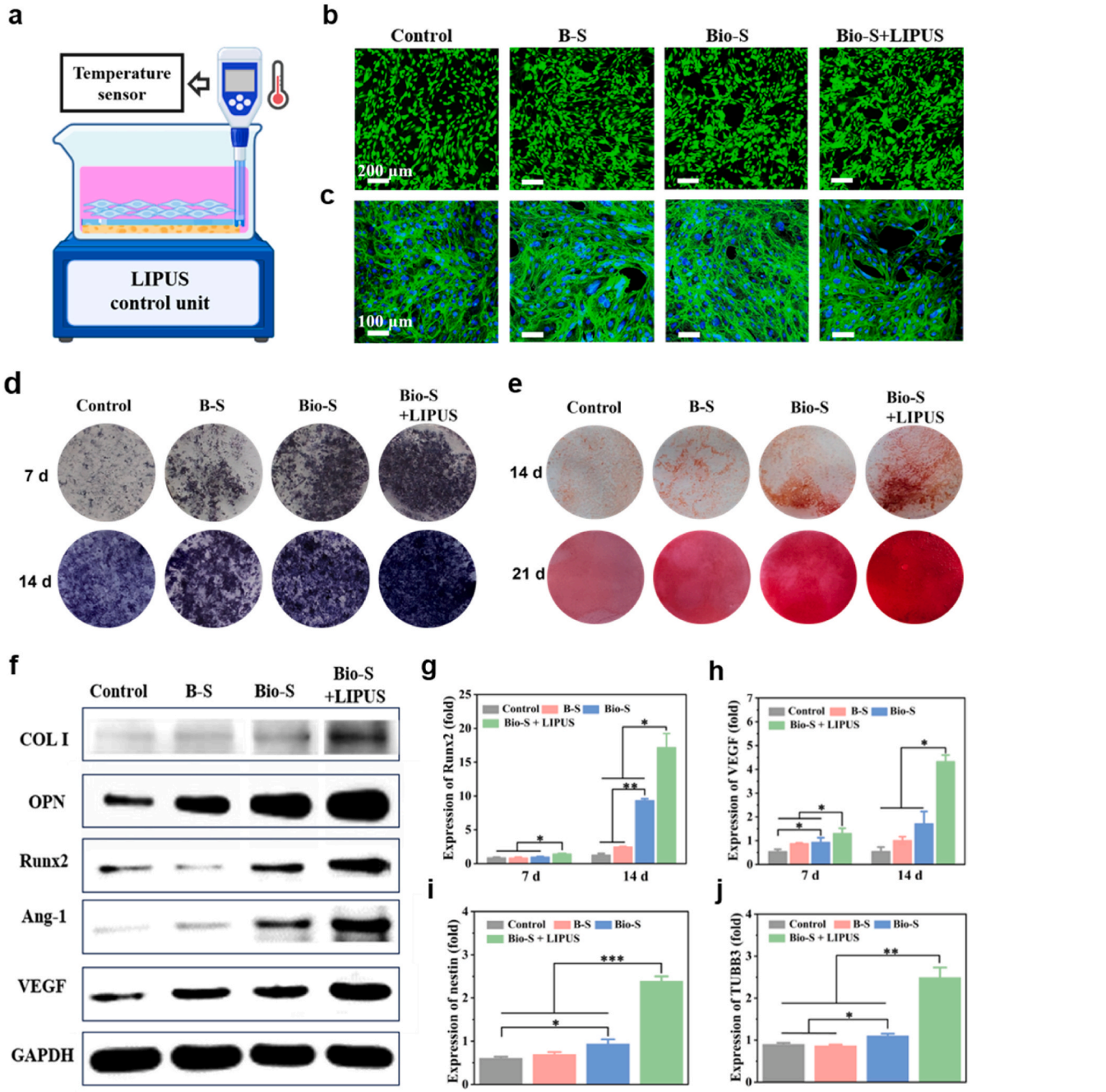

Fig. 3. Study on osteogenesis, angiogenesis, and neurogenesis of the scaffolds in vitro. a) Simplified schematic of cell culture under LIPUS-assisted piezoelectric stimulation. b) Live/dead and c) morphology fluorescence staining images of murine bone marrow mesenchymal stem cells (BMSCs) incubated with the control (cells without scaffold), B-S, Bio-S and Bio-S + LIPUS for 4 days (bars = 200 and 100 μm, respectively), green and red in Fig. (b) represent living cells and dead cells, respectively. F-actin and nucleus of cells in Fig. (c) exhibited blue and green fluorescence, respectively. Optical microscopy images of d) alkaline phosphatase (ALP) and e) alizarin red S (ARS) stained BMSCs in different groups. f) Western blotting of the expressions of osteogenic and angiogenic proteins in BMSCs cultured on different scaffolds for 14 days. GAPDH served as an internal control for equal loading. g-j) Relative mRNA expressions of Runx2, VEGF, nestin and TUBB3 in BMSCs treated by different groups. Data represent means ± standard deviations (n = 5). $^{*}P < 0.05$, $^{**}P < 0.01$, $^{***}P < 0.001$.

on the viability and differentiation of murine bone marrow mesenchymal stem cells (BMSCs) was investigated. The cells were incubated on top of the B-S, P-S, and Bio-S scaffolds, as well as the Bio-S scaffolds with LIPUS stimulation (Bio-S + LIPUS) (Fig. 3a). Cytocompatibility, crucial for the *in vivo* application of biomaterials, was evaluated in vitro for the different scaffolds. Fluorescence staining images revealed a gradual increase in the number of viable cells in each group from 2 days (Fig. S11) to 4 days (Fig. 3b). The cells exhibited a spindle-like spreading state (Fig. 3c). This morphological feature indicates that the materials in each group supported cell adhesion and growth on their surfaces. Cell proliferation, as measured by the CCK-8 assay, exceeded 100 % across all groups over 1, 3, 5, and 7 days (Fig. S12). These findings collectively show that LIPUS stimulation did not adversely affect cell viability. Consequently, the Bio-S bilayer scaffold is considered cytocompatible.

The early markers of osteogenic differentiation were subsequently examined using staining techniques such as alkaline phosphatase (ALP) and alizarin red S (ARS). The Bio-S group showed increased staining density from 7 to 14 days, compared to the B-S group and control group. Notably, under LIPUS-assisted piezoelectric stimulation, the staining density of the Bio-S + LIPUS group was significantly enhanced (Fig. 3d, Fig. S13a). Optical microscope images from ARS staining revealed increased calcium deposits in the B-S group. compared to the control group. More prominent deposits observed in the Bio-S group at both 14 and 21 days. The Bio-S + LIPUS group exhibited predominantly red stains, indicating a high deposition of calcium nodules (Fig. 3e, Fig. S13b). Results from ALP and ARS staining indicate that LIPUS-stimulated piezoelectric Bio-S induced higher ALP activity and calcium deposition. This plays a crucial role in enhancing osteogenic differentiation.

Osteogenesis-associated proteins and genes markers were evaluated to further validate the osteogenic potential of Bio-S combined with LIPUS stimulation. The levels of osteogenesis-associated proteins, including type I collagen (COL I), osteopontin (OPN), and the runt-related transcription factor 2 (Runx2), gradually increased from the B-S group to the Bio-S group and were even higher in the Bio-S + LIPUS group (Fig. 3f). Compared to the B-S group, the expression of COL1, OPN, and Runx2 genes in the Bio-S group was slightly elevated at both 7 and 14 days. However, in the Bio-S + LIPUS group, the expression levels of these genes at 14 days were significantly 2.7, 4.2, and 1.8 times higher, respectively, than those in the Bio-S group (Fig. 3g, Fig. S14). These findings demonstrate the potential of combining Bio-S with piezoelectric stimulation for bone regeneration.

Apart from osteogenesis, neurogenesis and angiogenesis are also essential for bone repair. Vascular and nerve infiltration into the wound site provides essential nutrients and communication signals for cell growth [51,52]. Accordingly, the angiogenic and neurogenic capabilities of Bio-S, with or without LIPUS stimulation, were evaluated. Qualitative analysis from Western blotting showed higher expression levels of vascular-associated proteins, Ang-1 and VEGF, in the Bio-S group, compared to the B-S group and control group (Fig. 3f). This finding suggests that Mg^{2+} released from PWH nanoparticles plays a pivotal role in promoting blood vessel formation [53]. When combined with LIPUS stimulation, the expression levels of these proteins further increased in the Bio-S + LIPUS group. This result is consistent with the gene expression results observed at both 7 and 14 days (Fig. 3h, Fig. S15a). After 14 days of co-culture, VEGF expression in the Bio-S group was 1.7 times higher that of the B-S group, but increased up to 4.3 times in the Bio-S + LIPUS group. These findings highlight that LIPUS-assisted piezoelectric stimulation, along with Mg^{2+} release from the periosteum-like layer, synergistically promotes angiogenesis.

Consistent with the angiogenesis studies, the Bio-S + LIPUS group also showed significantly upregulated expression of neuro-related genes, compared to other groups at 14 days (Fig. 3i, j, Fig. S15b). The expression levels of nestin, TUBB3, and NEFL in the Bio-S + LIPUS group were 2.6, 2.3, and 2.2 times higher, respectively, than those in the Bio-S group. These findings collectively suggest that Bio-S stimulated with LIPUS positively influences osteogenic, neurogenic, and angiogenic processes, making it highly effective for enhanced bone regeneration.

3.4. Osteogenic mechanism of Bio-S + LIPUS stimulation

Bioinformatics analysis of RNA transcriptome sequencing (RNA-seq) was conducted to investigate the osteogenic mechanism of Bio-S when stimulated by LIPUS. Differential expression gene (DEG) analysis showed that 1493 genes were upregulated and 1615 genes were downregulated in the Bio-S + LIPUS group (Fig. 4a). A volcano plot of the RNA-seq results further illustrated the distribution of DEGs (Fig. 4b). Kyoto encyclopedia of genes and genomes (KEGG) enrichment analysis of DEGs indicated significantly higher activity in the actin cytoskeleton, mitogen-activated protein kinase (MAPK) signaling pathways, HIF-1 signaling pathways, and neurotrophin signaling pathways in cells cultured on the Bio-S + LIPUS group (Fig. 4c).

Gene ontology (GO) analysis showed that Bio-S + LIPUS treatment significantly affected molecular functions such as glucose metabolic processes, ossification, axon extension, osteoblast differentiation, cellular response to hypoxia. It also impacted cellular components including microtubule, neuron-to-neuron synapses, axon parts, and dendritic spines, as well as biological processes like cadherin binding (Fig. S16). These variations were primarily involved in osteogenesis, angiogenesis, and neurogenesis. The results are consistent with the findings from KEGG analysis.

Electrical stimulation has been reported to enhance mitochondrial ATP production. The increase in ATP facilitates F-actin formation and remodeling that is critical in mediating osteogenesis [54]. The upregulated expression of Smad5 and P2X7 related genes in the heatmap indicates that piezoelectric stimulation significantly activated the ATP-related osteogenic energy metabolic pathway (Fig. 4d). Electrical stimulation and high calcium concentrations activate voltage-gated calcium channel (VGCC) and N-methyl-D-aspartic acid receptor (NMDAR) proteins on cell membranes, resulting in a raid increase Ca^{2+} influx. This influx, in turn, activates the calmodulin signaling pathway, which promotes nerve growth and activity [55,56]. Upregulation of calmodulin also induces the expression of calcineurin and nuclear factor of activated T-cells (NF-AT) genes, further accelerating osteogenesis. The significant expression of Ras, Raf, and RSK-related genes in the MAPK signaling pathway shows that Bio-S enhances nerve growth by activating both calmodulin and MKPK signaling pathways under piezoelectric stimulation. In addition, electrical stimulation and Mg^{2+} are crucial in regulating angiogenesis-associated PI3K-AKT and HIF-1 signaling pathways, respectively [57]. Specifically, Mg^{2+} modulates the transient receptor potential melastatin 7 (TRPM7) channel domain, which is essential for angiogenesis [58]. In the heatmap, upregulation in the expression of eIF4E, TFRC, HIF-1α, and PI3K-related genes was observed in the mentioned pathways. This finding indicates that piezoelectric stimulation of Mg^{2+} released from the Bio-S significantly promoted angiogenesis in the Bio-S + LIPUS group by activating PI3K-AKT and HIF-1 signaling pathways. These results suggest that Bio-S may enhance stem cell osteogenesis, neurogenesis, and angiogenesis by modulating mitochondrial ATP metabolism and the calmodu lin/calcineurin/NF-AT, calmodulin/MAPK/RSK, PI3K-AKT/VEGF and HIF-1 related signaling pathways under piezoelectric stimulation (Fig. 4e).

To further elucidate the biological mechanism of Bio-S + LIPUS, the major genes involved in the aforementioned signaling pathways, including P2X7, HIF-1α, OCN, and RSK were examined at 14 days using RT-qPCR (Fig. 4f–h, Fig. S17). Compared to the B-S group and control group, the expression levels of P2X7, OCN, and HIF-1α genes was higher in the Bio-S group. This was even more so when Bio-S was stimulated with LIPUS. Western blot analysis revealed elevated phosphorylation levels of MEK, ERK, PI3K, and AKT in the Bio-S group, implicating the MEK-ERK and PI3K-AKT pathways. Voltage-gated Ca^{2+} influx could phosphorylate downstream proteins in the MEK-ERK pathway,

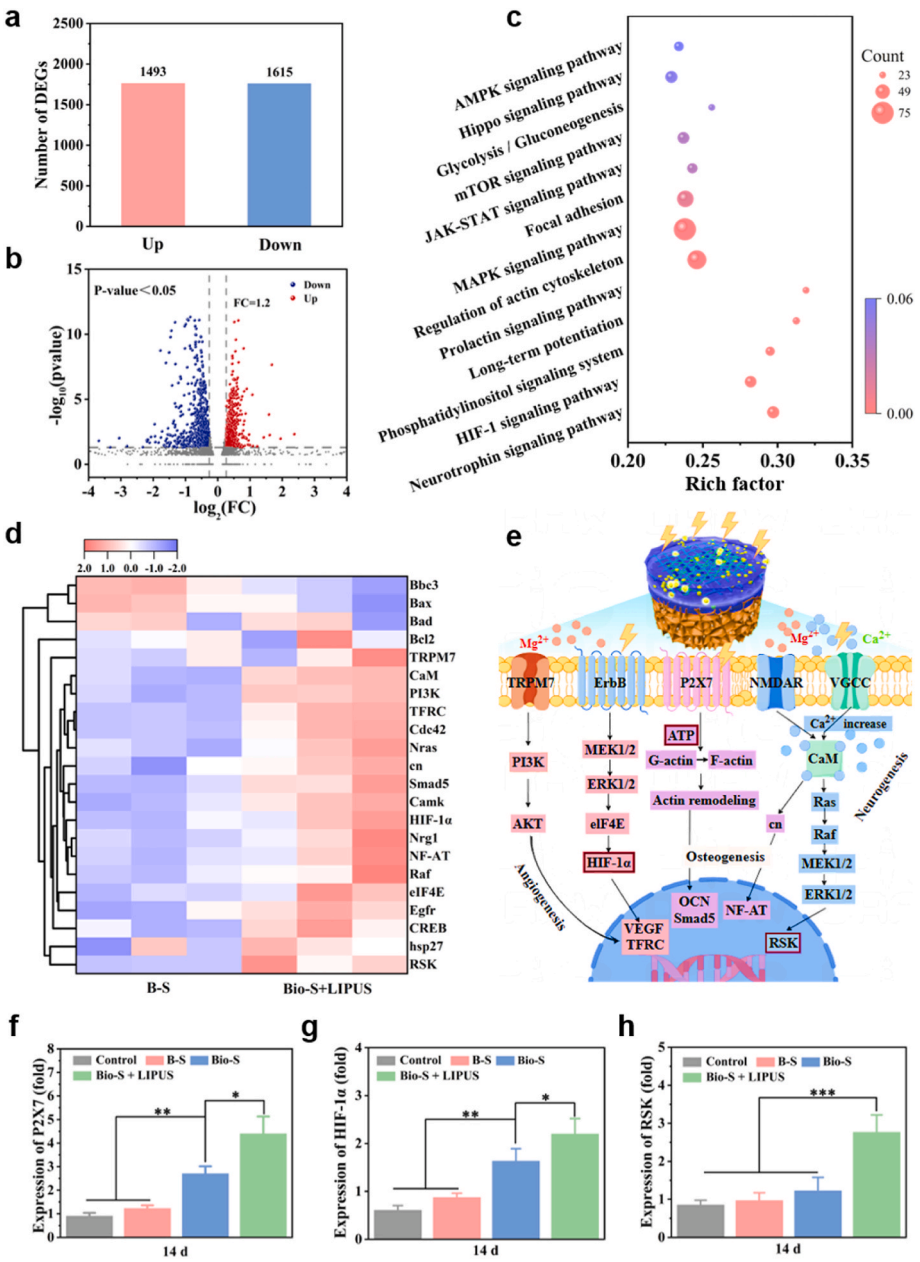

Fig. 4. Investigation of the mechanism of osteogenesis. a) The number of upregulated and downregulated genes. b) Volcano plot depicting the transcriptomic results for differentially expressed genes identified in the Bio-S + LIPUS group compared to the B-S group, based on a fold change of 1.2 and $p < 0.05$. c) Kyoto encyclopedia of genes and genomes (KEGG) enrichment analysis and d) hierarchical cluster heatmap of DEGs in the B-S and Bio-S + LIPUS groups. e) Schematic of angiogenesis, neurogenesis and osteogenesis. f-h) Relative mRNA expressions of P2X7, HIF-1α, and RSK in BMSCs. Bars represent means ± standard deviations (n = 5). $^{*}P < 0.05$, $^{**}P < 0.01$, $^{***}P < 0.001$.

regulating neuronal activity and axonal growth. Additionally, magnesium ions and electrical signal stimulation phosphorylate proteins in both the PI3K-AKT and MEK-ERK pathways, affecting the expression of vascular growth factor VEGF and hypoxia-inducible factor HIF-1α, thereby promoting angiogenesis (Fig. S18). This observation indicates that the synergistic effect of functional ion (Mg^{2+}, Ca^{2+}) released from Bio-S, combined with piezoelectric stimulation, enhances osteogenesis and angiogenesis in BMSCs. Furthermore, the gene expression of RSK was significantly upregulated in the Bio-S + LIPUS group, while it remained low in other groups. This marked difference indicates that LIPUS-assisted piezoelectric stimulation markedly promotes neurogenesis. Consistent with the RNA-seq findings, Bio-S effectively promotes osteogenesis, angiogenesis, and neurogenesis by activating the PI3K-AKT, HIF-1, ATP, MAPK, and Ca^{2+} signaling pathways under LIPUS stimulation. Taken together, Bio-S with piezoelectric stimulation demonstrates strong osteogenic, angiogenic, and neurogenic differentiation potential during bone defect repair.

3.5. *In vivo* bone regeneration potential of Bio-S

The *in vivo* efficacy of Bio-S + LIPUS was further examined using a rat calvaria defect model. Details of the surgical procedure and material implantation process are included in the supplementary materials (Fig. S19). To evaluate the response of native bone tissue to the implanted materials, the reparative effect at the defect site was examined after 8 weeks post-implantation using micro computed tomography (Fig. 5a). Coronal images revealed reduction in the defect area in the B-S group, compared to the control group. This is primarily attributed to the

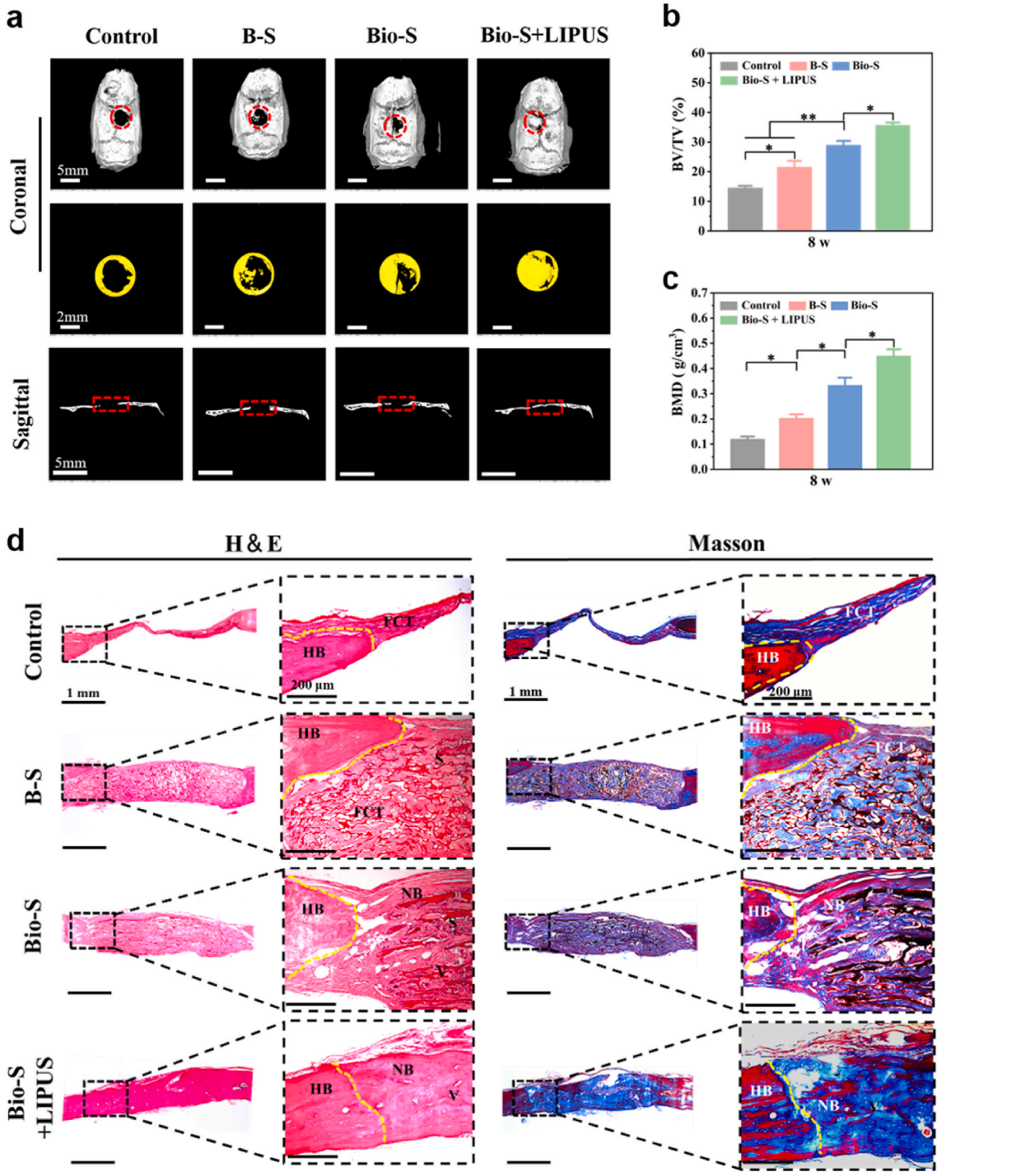

Fig. 5. In vivo repair of the different scaffolds after 8 weeks of implantation into calvarial bone defects. a) 3D reconstruction of the coronal and sagittal planes of the skull (red circles and rectangle: initial defects. Yellow area: new bone filling) (Bars = 5 mm and 2 mm, respectively). Quantitative analysis of b) bone volume/tissue volume (BV/TV) and c) bone density (BMD) of the defects from different groups. d) H&E and Masson's trichrome staining of the implanted sites at different magnification (S: scaffold; HB: host bone; V: vessel; NB: new bone; FCT: fibrous tissue; Yellow dashed line: demarcation between host and regenerated bone tissues) (Bars = 1 mm and 200 μm, respectively). Error bars: Means ± standard deviations (n = 5). *$P < 0.05$, **$P < 0.01$.

in-situ crystallization of HAp nanoparticles. This outcome is consistent with previous findings that highlight the strong osteogenic activity of calcium phosphate materials [59,60].

In contrast, the Bio-S group showed more extensive bone repair. Defects were almost fully covered by newly-formed bone in the Bio-S + LIPUS group. The new bone grew from the edges toward the center of the defect, forming an integrated structure with the native bone, as observed in sagittal views of the Bio-S + LIPUS group. Previous studies indicate that Mg^{2+} promotes angiogenesis, while electrical stimulation induces cell proliferation and osteogenic differentiation [61]. Therefore, it is reasonable to speculate that the excellent bone repair observed in the Bio-S + LIPUS group results from the synergistic effect of Mg^{2+}

release from Bio-S, and LIPUS-assisted piezoelectric stimulation.

Quantitative analysis of new bone formation identified that the values of new bone volume/tissue volume (BV/TV) (Fig. 5b) and bone mineral density (BMD) (Fig. 5c) were lower in the B-S group (21.5 %, 0.20 g/cm^3). This was followed by the Bio-S group (29.1 %, 0.33 g/cm^3), and highest in the Bio-S + LIPUS group (35.7 %, 0.45 g/cm^3). All of these values were higher than that of control group. These results indicate that the Bio-S + LIPUS group possesses optimal osteogenic ability. This finding is consistent with the tissue reconstruction results mentioned earlier. Osteogenic parameter values of the bilayer scaffolds are significantly higher than those previously reported bone tissue engineered scaffolds [16,46,62]. The enhanced repair effects of bone defects maybe mainly attributed to the special structural and bioactive composition as well as the piezoelectricity of the bioinspired scaffold.

Eight weeks after implantation, H&E and Masson's trichrome staining were used to visualize new bone formation in defect sites (Fig. 5d). In the control group (without scaffold), there was minimal connective fibrous tissue between the newly-formed tissue and native host tissues. In contrast, the areas of new tissue regeneration in the material transplantation groups were significantly increased. The newly-formed tissue in the B-S group was relatively loose, consisting mainly of immature fibrous tissue. In comparison, the Bio-S group exhibited a higher level of new bone formation. The Bio-S + LIPUS group showed the best performance. In this group, some vessel tissues were visible at low magnification, indicating the formation of mature osseous tissue [63]. Masson's trichrome staining showed that the control group had narrower and looser collagen fibrils, whereas the B-S group showed slightly improved collagen fibril deposition. The Bio-S group exhibited a significant increase in newly-formed mature collagen fibrils. This feature was further enhanced in the Bio-S + LIPUS group due to LIPUS-assisted piezoelectric stimulation. This highlights the crucial role of collagen matrix development and blood vessel formation in the rehabilitation of critical-sized bone defects. The improved osteogenic performance of Bio-S may be attributed to its 3D hierarchical porous structure and active composition, including HAp and PWH nanoparticles. In addition, reconstructing the bioelectric microenvironment of the defects periosteum synergistically promoted stem cell recruitment, growth, and their osteogenic differentiation.

An important aspect of bone repair involves blood vessels and neural networks. The nervous system enhances osteoblast differentiation,

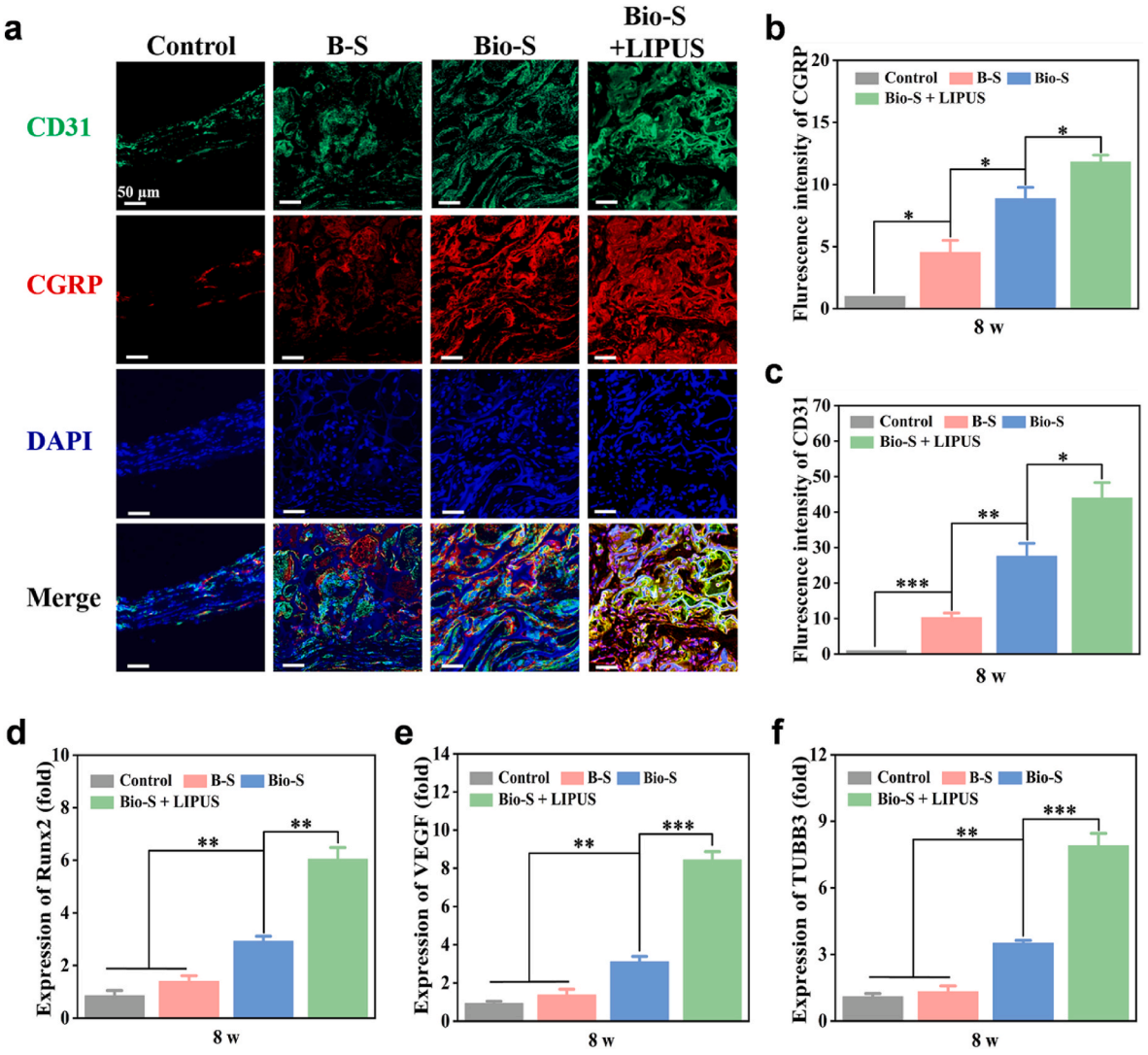

Fig. 6. Analysis of osteogenesis, angiogenesis, and neurogenesis *in vivo*. a) Representative immunofluorescence images and b-c) fluorescence intensity bar charts of CD31 (green) and CGRP (red) in the defect areas after 8 weeks of implantation (Bar = 5 μm). d-f) Expression of osteogenic, angiogenic, and neurogenic genes in the newly-formed tissue after 8 weeks of implantation into the calvarial bone defects. Error bars: Means ± standard deviations (n = 5). *$P < 0.05$, **$P < 0.01$, ***$P < 0.001$.

activity, and defect remodeling by releasing neuropeptides. Blood vessels transport nutrients from surrounding tissues to the defect to promote cellular activity [7,51]. To study tissue angiogenesis and neurogenesis, immunofluorescence staining was performed on tissue sections from various experimental groups. CD31, also known as platelet endothelial cell adhesion molecule, is a prominent marker for endothelial cells [64]. Calcitonin gene-related polypeptide (CGRP), produced by nerve cells, activate CGRP receptors in osteoblasts to induce osteogenic differentiation [65]. Hence, CD31 and CGRP were employed for assessing angiogenic and neurogenic responses to the implants, and visualized in red and green fluorescence, respectively (Fig. 6a). The intensity and density of fluorescence increased progressively from the control to B-S, to Bio-S, to Bio-S + LIPUS group. The results are consistent with the results of the statistical analysis of fluorescence intensity (Fig. 6b and c). In addition, as shown in Fig. S20, immunohistochemical staining for neural (CGRP) and vascular (CD31) markers exhibited the most pronounced positive expression in the Bio-S + LIPUS group (where shades of brown represent the intensity of protein expression). These strongly demonstrate the superior angiogenic and neurogenic potential of the Bio-S + LIPUS group.

To further quantify the reparative effects on defective bone tissue, RT-qPCR analysis was used to measure the expression levels of osteogenic (COL I, Runx2), angiogenic (VEGF), and neurogenic (TUBB3) genes at the defect sites (Fig. 6d–f, Fig. S21). Compared to the B-S and control groups, all genes exhibited increased expression in the Bio-S group, with even higher expression levels under LIPUS stimulation. Specifically, compared to the B-S group, fold changes in the Bio-S group were 3.1 folds for COL I, 2.1 folds for Runx2, 2.3 folds for VEGF, and 2.6 folds for TUBB3. These values increased to 4.3, 8.3, 6.2, and 5.9 folds, respectively, in the Bio-S + LIPUS group. The enhanced outcomes observed in the Bio-S + LIPUS group are likely attributable to the combined effects of Mg^{2+} release and the piezoelectric properties of the Bio-S scaffold, which promote nerve and blood vessel formation. Taken together, the Bio-S bilayer scaffold with piezoelectric stimulation is effective for neuro-vascularized bone regeneration.

4. Conclusion

Inspired by the hierarchical structure and function of natural periosteum-bone, a novel Bio-S scaffold with enhanced piezoelectric properties was developed for the repair of critical-sized bone effects. The lower B-S layer of the scaffold exhibited a bone-like 3D porous structure and a biomineralized HAp active composition. In contrast, the upper P-S layer, a double network hydrogel hybridized with PWH nanoparticles, demonstrated periosteum-like viscoelasticity and an optimal osteogenic piezoelectric coefficient. The scaffold's mechanical interlocking structure and chemical covalent bonds created a robust and integrated interface similar to the embedding pattern of Sharpey's fibers between the periosteum and bone matrix. This design provides a biomimetic, spatially-stable environment for cell growth. Unlike conventional B-S scaffolds, the Bio-S scaffold, particularly when paired with LIPUS-assisted piezoelectric stimulation, effectively promoted osteogenesis, angiogenesis, and neurogenesis. This was achieved by activating the PI3K-AKT, HIF-1, ATP, MAPK, and Ca^{2+} signaling pathways. These mechanisms significantly enhanced the regeneration of cranial bone defects in rats. The Bio-S, with its endogenous piezoelectric stimulation, demonstrates remarkable potential for neuro-vascularized bone regeneration. This bilayer scaffold may act as a self-powered electrical stimulator to expedite bone regeneration under dynamic physical conditions. Noteworthily, the degradation of prepared materials inherently impacts scaffold piezoelectric properties. Therefore, optimizing the degradation rate of piezoelectric materials to align with bone regeneration is crucial for advancing future neurovascular bone regeneration.

CRediT authorship contribution statement

Yao Zhao: Writing – review & editing, Writing – original draft, Supervision, Resources, Project administration, Funding acquisition, Formal analysis, Data curation, Conceptualization. **Yunfan Cai:** Visualization, Software, Methodology, Investigation, Formal analysis, Data curation. **Wenkai Wang:** Software, Methodology. **Yongkang Bai:** Visualization, Resources. **Mingyi Liu:** Validation, Software, Methodology. **Yan Wang:** Methodology, Investigation. **Wen Niu:** Validation, Resources. **Zhixiao Luo:** Validation, Supervision, Resources. **Lingyun Xia:** Visualization, Resources. **Juanfang Zhu:** Resources, Methodology. **Fei Zhao:** Formal analysis, Data curation. **Franklin R. Tay:** Writing – review & editing, Resources. **Lina Niu:** Writing – review & editing, Supervision, Resources, Project administration.

Ethics approval and consent to participate

This work does not contain results related to human participant.

All experimental protocols in this work met the National Institute of Health guidelines for the care and use of laboratory animals, and were reviewed and approved by the Institutional Animal Care and Use Committee of the Fourth Military Medical University (IACUC-2023-kq-029).

Declaration of competing interest

The authors declare no conflict of interest.

Acknowledgments

The authors acknowledge financial support from the National Natural Science Foundation of China (82325012), National Key Research and Development Program of China (2022YFC2405900, 2022YFC2405901), China Postdoctoral Science Foundation (2024M754272), Natural Science Basic Research Program of Shaanxi (2024JC-YBQN-0804), Postdoctoral Research Fund of the Fourth Military Medical University (lj202220110) and the Shaanxi Key Scientific and Technological Innovation Team (2020TD-033) and by the Youth Innovation Team of Shaanxi Universities.

Appendix A. Supplementary data

Supplementary data to this article can be found online at https://doi.org/10.1016/j.bioactmat.2024.10.020.

References

[1] Y. He, F. Li, P. Jiang, F. Cai, Q. Lin, M. Zhou, H. Liu, F. Yan, Remote control of the recruitment and capture of endogenous stem cells by ultrasound for in situ repair of bone defects, Bioact. Mater. 21 (2023) 223–238.
[2] A.P. Kusumbe, S.K. Ramasamy, R.H. Adams, Coupling of angiogenesis and osteogenesis by a specific vessel subtype in bone, Nature 507 (7492) (2014) 323–328.
[3] T. Fukuda, S. Takeda, R. Xu, H. Ochi, S. Sunamura, T. Sato, S. Shibata, Y. Yoshida, Z. Gu, A. Kimura, C. Ma, C. Xu, W. Bando, K. Fujita, K. Shinomiya, T. Hirai, Y. Asou, M. Enomoto, H. Okano, A. Okawa, H. Itoh, Sema3A regulates bone-mass accrual through sensory innervations, Nature 497 (7450) (2013) 490–493.
[4] L. Zhang, N. Liu, J. Shao, D. Gao, Y. Liu, Y. Zhao, C. Han, D. Chen, L. Wang, W. W. Lu, F. Yang, Bidirectional control of parathyroid hormone and bone mass by subfornical organ, Neuron 111 (12) (2023) 1914–1932.
[5] X. Lv, F. Gao, X. Cao, Skeletal interoception in bone homeostasis and pain, Cell Metabol. 34 (12) (2022) 1914–1931.
[6] Q.Q. Wan, W.P. Qin, Y.X. Ma, M.J. Shen, J. Li, Z.B. Zhang, J.H. Chen, F.R. Tay, L. N. Niu, K. Jiao, Crosstalk between bone and nerves within bone, Adv. Sci. 8 (7) (2021) 2003390.
[7] X. Han, Q. Saiding, X. Cai, Y. Xiao, P. Wang, Z. Cai, X. Gong, W. Gong, X. Zhang, W. Cui, Intelligent vascularized 3D/4D/5D/6D-printed tissue scaffolds, Nano-Micro Lett. 15 (1) (2023) 1–43.
[8] H. Cui, W. Zhu, B. Holmes, L.G. Zhang, Biologically inspired smart release system based on 3D bioprinted perfused scaffold for vascularized tissue regeneration, Adv. Sci. 3 (8) (2016) 1600058.

[9] Y. Xia, X. Jing, X. Wu, P. Zhuang, X. Guo, H. Dai, 3D-printed dual-ion chronological release functional platform reconstructs neuro-vascularization network for critical-sized bone defect regeneration, Chem. Eng. J. 465 (2023) 143015.
[10] C. Lian, J. Liu, W. Wei, X. Wu, T. Goto, H. Li, R. Tu, H. Dai, Mg-gallate metal-organic framework-based sprayable hydrogel for continuously regulating oxidative stress microenvironment and promoting neurovascular network reconstruction in diabetic wounds, Bioact. Mater. 38 (2024) 181–194.
[11] Y. Zhao, S. Zhao, Z. Ma, C. Ding, J. Chen, J. Li, Chitosan-based scaffolds for facilitated endogenous bone re-generation, Pharmaceuticals 15 (8) (2022) 1023.
[12] L. Kuang, J. Huang, Y. Liu, X. Li, Y. Yuan, C. Liu, Injectable hydrogel with NIR light-responsive, dual-mode PTH release for osteoregeneration in osteoporosis, Adv. Funct. Mater. 31 (47) (2021) 2105383.
[13] M.N. Collins, G. Ren, K. Young, S. Pina, R.L. Reis, J.M. Oliveira, Scaffold fabrication technologies and structure/function properties in bone tissue engineering, Adv. Funct. Mater. 31 (21) (2021) 2010609.
[14] Y. Xu, C. Xu, L. He, J. Zhou, T. Chen, L. Ouyang, X. Guo, Y. Qu, Z. Luo, D. Duan, Stratified-structural hydrogel incorporated with magnesium-ion-modified black phosphorus nanosheets for promoting neuro-vascularized bone regeneration, Bioact. Mater. 16 (2) (2022) 271–284.
[15] L. Laijun, Z. Yu, L. Chaojing, M. Jifu, W. Fujun, W. Lu, An enhanced periosteum structure/function dual mimicking membrane forin-siturestorations of periosteum and bone, Biofabrication 13 (3) (2021) 33878742.
[16] F. Zhao, C. Zhang, J. Liu, L. Liu, X. Cao, X. Chen, B. Lei, L. Shao, Periosteum structure/function-mimicking bioactive scaffolds with piezoelectric/chem/nano signals for critical-sized bone regeneration, Chem. Eng. J. 402 (2) (2020) 126203.
[17] L.-n. Niu, S.E. Jee, K. Jiao, L. Tonggu, M. Li, L. Wang, Y.-d. Yang, J.-h. Bian, L. Breschi, S.S. Jang, J.-h. Chen, David H. Pashley, Franklin R. Tay, Collagen intrafibrillar mineralization as a result of the balance between osmotic equilibrium and electroneutrality, Nat. Mater. 16 (3) (2017) 370–378.
[18] J.C. Anderson, C. Eriksson, Electrical properties of wet collagen, Nature 218 (5137) (1968) 166–168.
[19] C. Zhang, W. Liu, C. Cao, F. Zhang, Q. Tang, S. Ma, J. Zhao, L. Hu, Y. Shen, L. Chen, Modulating surface potential by controlling the β phase content in poly(vinylidene fluoridetrifluoroethylene) membranes enhances bone regeneration, Adv. Funct. Mater. 7 (11) (2018) 1701466.
[20] Z. Liu, X. Wan, Z.L. Wang, L. Li, Electroactive biomaterials and systems for cell fate determination and tissue regeneration: design and applications, Adv. Mater. 33 (32) (2021) 2007429.
[21] Y. Zhang, J. Xu, Y.C. Ruan, M.K. Yu, M. O'Laughlin, H. Wise, D. Chen, L. Tian, D. Shi, J. Wang, S. Chen, J.Q. Feng, D.H.K. Chow, X. Xie, L. Zheng, L. Huang, S. Huang, K. Leung, N. Lu, L. Zhao, H. Li, D. Zhao, X. Guo, K. Chan, F. Witte, H. C. Chan, Y. Zheng, L. Qin, Implant-derived magnesium induces local neuronal production of CGRP to improve bone-fracture healing in rats, Nat. Med. 22 (10) (2016) 1160–1169.
[22] Y. Su, L. Zeng, R. Deng, B. Ye, S. Tang, Z. Xiong, T. Sun, Q. Ding, W. Su, X. Jing, Q. Gao, X. Wang, Z. Qiu, K. Chen, D. Quan, X. Guo, Endogenous electric field-coupled PD@BP biomimetic periosteum promotes bone regeneration through sensory nerve via fanconi anemia signaling pathway, Adv. Healthcare Mater. 12 (12) (2023) 2203027.
[23] Y. Wei, M. Ju, F. Zheng, S. Wei, S. Han, S. Lu, R. Liu, H. Wu, Cuttlebone-derived organic matrix: a facile periosteum substitute for bone regeneration, Adv. Funct. Mater. 33 (31) (2023) 2214095.
[24] C. Liu, Y. Lou, Z. Sun, H. Ma, M. Sun, S. Li, D. You, J. Wu, B. Ying, W. Ding, M. Yu, H. Wang, 4D printing of personalized-tunable biomimetic periosteum with anisotropic microstructure for accelerated vascularization and bone healing, Adv. Healthcare Mater. 12 (22) (2023) 2202868.
[25] G. Yang, H. Liu, Y. Cui, J. Li, X. Zhou, N. Wang, F. Wu, Y. Li, Y. Liu, X. Jiang, S. Zhang, Bioinspired membrane provides periosteum-mimetic microenvironment for accelerating vascularized bone regeneration, Biomaterials 268 (2021) 120561.
[26] X. Zhang, C. Xie, A.S. Lin, H. Ito, H. Awad, J.R. Lieberman, P.T. Rubery, E. M. Schwarz, R.J. O'Keefe, R.E. Guldberg, Periosteal progenitor cell fate in segmental cortical bone graft transplantations: implications for functional tissue engineering, J. Bone Miner. Res. 20 (12) (2005) 2124–2137.
[27] S. Liu, L. Zhang, Z. Li, F. Gao, Q. Zhang, A. Bianco, H. Liu, S. Ge, B. Ma, Materials-mediated in situ physical cues for bone regeneration, Adv. Funct. Mater. 34 (1) (2024) 2306534.
[28] Z. Li, D. He, B. Guo, Z. Wang, H. Yu, Y. Wang, S. Jin, M. Yu, L. Zhu, L. Chen, C. Ding, X. Wu, T. Wu, S. Gong, J. Mao, Y. Zhou, D. Luo, Y. Liu, Self-promoted electroactive biomimetic mineralized scaffolds for bacteria-infected bone regeneration, Nat. Commun. 14 (1) (2023) 6963.
[29] D. Khare, B. Basu, A.K. Dubey, Electrical stimulation and piezoelectric biomaterials for bone tissue engineering applications, Biomaterials 258 (2020) 120280.
[30] Z.L. Wang, G. Zhu, Y. Yang, S. Wang, C. Pan, Progress in nanogenerators for portable electronics, Mater. Today 15 (12) (2012) 532–543.
[31] F. Yang, J. Li, Y. Long, Z. Zhang, L. Wang, J. Sui, Y. Dong, Y. Wang, R. Taylor, D. Ni, W. Cai, P. Wang, T. Hacker, X. Wang, Wafer-scale heterostructured piezoelectric bio-organic thin films, Science 373 (6552) (2021) 337–342.
[32] Y. Liu, G. Dzidotor, T.T. Le, T. Vinikoor, K. Morgan, E.J. Curry, R. Das, A. McClinton, E. Eisenberg, L.N. Apuzzo, K.T.M. Tran, P. Prasad, T.J. Flanagan, S.-W. Lee, H.-M. Kan, M.T. Chorsi, K.W.H. Lo, C.T. Laurencin, T.D. Nguyen, Exercise-induced piezoelectric stimulation for cartilage regeneration in rabbits, Sci. Transl. Med. 14 (627) (2022) eabi7282.
[33] A.P. Sarvazyan, O.V. Rudenko, M. Fatemi, Acoustic radiation force: a review of four mechanisms for biomedical applications, IEEE Trans. Ultrason. Ferroelectrics Freq. Control 68 (11) (2021) 3261–3269.
[34] A. Kim, S.K. Lee, T. Parupudi, R. Rahimi, S.H. Song, M.C. Park, S. Islam, J. Zhou, A. K. Majumdar, J.S. Park, J.M. Yoo, B. Ziaie, An ultrasonically powered implantable microprobe for electrolytic ablation, Sci. Rep. 10 (1) (2020) 1510.
[35] S. Metwally, U. Stachewicz, Surface potential and charges impact on cell responses on biomaterials interfaces for medical applications, Mater. Sci. Eng. C 104 (2019) 109883.
[36] Z. Qiao, M. Lian, X. Liu, X. Zhang, Y. Han, B. Ni, R. Xu, B. Yu, Q. Xu, K. Dai, Electreted sandwich membranes with persistent electrical stimulation for enhanced bone regeneration, ACS Appl. Mater. Interfaces 14 (28) (2022) 31655–31666.
[37] G. Li, Z. Li, Y. Min, S. Chen, R. Han, Z. Zhao, 3D-printed piezoelectric scaffolds with shape memory polymer for bone regeneration, Small 19 (40) (2023) 2302927.
[38] S. Onuora, Electric scaffolds charge cartilage repair, Nat. Rev. Rheumatol. 18 (3) (2022), 127-127.
[39] T. Vinikoor, G.K. Dzidotor, T.T. Le, Y. Liu, H.-M. Kan, S. Barui, M.T. Chorsi, E. J. Curry, E. Reinhardt, H. Wang, P. Singh, M.A. Merriman, E. D'Orio, J. Park, S. Xiao, J.H. Chapman, F. Lin, C.-S. Truong, S. Prasadh, L. Chuba, S. Killoh, S.-W. Lee, Q. Wu, R.M. Chidambaram, K.W.H. Lo, C.T. Laurencin, T.D. Nguyen, Injectable and biodegradable piezoelectric hydrogel for osteoarthritis treatment, Nat. Commun. 14 (1) (2023) 6257.
[40] H.L. Jang, K. Jin, J. Lee, Y. Kim, S.H. Nahm, K.S. Hong, K.T. Nam, Revisiting whitlockite, the second most abundant biomineral in bone: nanocrystal synthesis in physiologically relevant conditions and biocompatibility evaluation, ACS Nano 8 (1) (2014) 634–641.
[41] V.K. Kaliannagounder, N.P.M.J. Raj, A.R. Unnithan, J. Park, S.S. Park, S.-J. Kim, C. H. Park, C.S. Kim, A.R.K. Sasikala, Remotely controlled self-powering electrical stimulators for osteogenic differentiation using bone inspired bioactive piezoelectric whitlockite nanoparticles, Nano Energy 85 (62) (2021) 105901.
[42] V.K. Kaliannagounder, N.P.M.J. Raj, A.R. Unnithan, J. Park, S.S. Park, S.-J. Kim, C. H. Park, C.S. Kim, A.R.K. Sasikala, Remotely controlled self-powering electrical stimulators for osteogenic differentiation using bone inspired bioactive piezoelectric whitlockite nanoparticles, Nano Energy 85 (2021) 105901.
[43] P. Chen, C. Xu, P. Wu, K. Liu, F. Chen, Y. Chen, H. Dai, Z. Luo, Wirelessly powered electrical-stimulation based on biodegradable 3D piezoelectric scaffolds promotes the spinal cord injury repair, ACS Nano 16 (10) (2022) 16513–16528.
[44] L. Wu, Y. Gu, L. Liu, J. Tang, J. Mao, K. Xi, Z. Jiang, Y. Zhou, Y. Xu, L. Deng, L. Chen, W. Cui, Hierarchical micro/nanofibrous membranes of sustained releasing VEGF for periosteal regeneration, Biomaterials 227 (1) (2020) 119555.
[45] X. Li, L. He, Y. Li, M. Chao, M. Li, P. Wan, L. Zhang, Healable, degradable, and conductive MXene nanocomposite hydrogel for multifunctional epidermal sensors, ACS Nano 15 (4) (2021) 7765–7773.
[46] Y. Zhao, T. Fan, J. Chen, J. Su, X. Zhi, P. Pan, L. Zou, Q. Zhang, Magnetic bioinspired micro/nanostructured composite scaffold for bone regeneration, Colloids Surf., B 174 (2019) 70–79.
[47] J.E. Aaron, Periosteal Sharpey's fibers: a novel bone matrix regulatory system? Front. Endocrinol. 3 (9) (2012) 1–10.
[48] Y. Zhao, X. Peng, D. Wang, H. Zhang, Q. Xin, M. Wu, X. Xu, F. Sun, Z. Xing, L. Wang, P. Yu, J. Xie, J. Li, H. Tan, C. Ding, J. Li, Chloroplast-inspired scaffold for infected bone defect therapy: towards stable photothermal properties and self-defensive functionality, Adv. Sci. 9 (31) (2022) 2204535.
[49] Z. Tao, Z. Yuan, D. Zhou, L. Qin, L. Xiao, S. Zhang, C. Liu, J. Zhao, Y. Li, Fabrication of magnesium-doped porous polylactic acid microsphere for bone regeneration, Biomater. Transl. 4 (4) (2023) 280–290.
[50] J. Wang, F. Witte, T. Xi, Y. Zheng, K. Yang, Y. Yang, D. Zhao, J. Meng, Y. Li, W. Li, K. Chan, L. Qin, Recommendation for modifying current cytotoxicity testing standards for biodegradable magnesium-based materials, Acta Biomater. 21 (2015) 237–249.
[51] Q. Qin, S. Lee, N. Patel, K. Walden, M. Gomez-Salazar, B. Levi, A.W. James, Neurovascular coupling in bone regeneration, Exp. Mol. Med. 54 (11) (2022) 1844–1849.
[52] S. Li, L. Zhang, C. Liu, J. Kim, K. Su, T. Chen, L. Zhao, X. Lu, H. Zhang, Y. Cui, X. Cui, F. Yuan, H. Pan, Spontaneous immunomodulation and regulation of angiogenesis and osteogenesis by Sr/Cu-borosilicate glass (BSG) bone cement to repair critical bone defects, Bioact. Mater. 23 (5) (2023) 101–117.
[53] F. Shams, H. Moravvej, S. Hosseinzadeh, E. Mostafavi, H. Bayat, B. Kazemi, M. Bandehpour, E. Rostami, A. Rahimpour, H. Moosavian, Overexpression of VEGF in dermal fibroblast cells accelerates the angiogenesis and wound healing function: in vitro and in vivo studies, Sci. Rep. 12 (1) (2022) 18529.
[54] T. Zhou, L. Yan, C. Xie, P. Li, L. Jiang, J. Fang, C. Zhao, F. Ren, K. Wang, Y. Wang, H. Zhang, T. Guo, X. Lu, A mussel-inspired persistent ROS-scavenging, electroactive, and osteoinductive scaffold based on electrochemical-driven in situ nanoassembly, Small 15 (25) (2019) 1805440.
[55] J.P. Dupuis, O. Nicole, L. Groc, NMDA receptor functions in health and disease: old actor, new dimensions, Neuron 111 (15) (2023) 2312–2328.
[56] B.A. Simms, G.W. Zamponi, Neuronal voltage-gated calcium channels: structure, function, and dysfunction, Neuron 82 (1) (2014) 24–45.
[57] A. Citri, Y. Yarden, EGF–ERBB signalling: towards the systems level, Nat. Rev. Mol. Cell Biol. 7 (7) (2006) 505–516.
[58] K.D. Nadezhdin, L. Correia, C. Narangoda, D.S. Patel, A. Neuberger, T. Gudermann, M.G. Kurnikova, V. Chubanov, A.I. Sobolevsky, Structural mechanisms of TRPM7 activation and inhibition, Nat. Commun. 14 (1) (2023) 2639.
[59] K. Zhou, P. Yu, X. Shi, T. Ling, W. Zeng, A. Chen, W. Yang, Z. Zhou, Hierarchically porous hydroxyapatite hybrid scaffold incorporated with reduced graphene oxide for rapid bone ingrowth and repair, ACS Nano 13 (8) (2019) 9595–9606.
[60] K. Liang, C. Zhao, C. Song, L. Zhao, P. Qiu, S. Wang, J. Zhu, Z. Gong, Z. Liu, R. Tang, X. Fang, Y. Zhao, In situ biomimetic mineralization of bone-like

hydroxyapatite in hydrogel for the acceleration of bone regeneration, ACS Appl. Mater. Interfaces 15 (1) (2023) 292–308.
[61] T. Wang, H. Ouyang, Y. Luo, J. Xue, E. Wang, L. Zhang, Z. Zhou, Z. Liu, X. Li, S. Tan, Y. Chen, L. Nan, W. Cao, Z. Li, F. Chen, L. Zheng, Rehabilitation exercise-driven symbiotic electrical stimulation system accelerating bone regeneration, Sci. Adv. 10 (1) (2024) eadi6799.
[62] Y. Zhao, J. Chen, L. Zou, G. Xu, Y. Geng, Facile one-step bioinspired mineralization by chitosan functionalized with graphene oxide to activate bone endogenous regeneration, Chem. Eng. J. 378 (2019) (2019) 122174.
[63] P. Pan, Y. Geng, L. Hu, Q. Liu, M. Liu, M. Cheng, L. Chen, J. Chen, Biologically enhanced 3D printed micro-nano hybrid scaffolds doped with abalone shell for bone regeneration, Adv. Compos. Hybrid Mater. 6 (1) (2022) 10–19.
[64] K.C.P. Cheung, S. Fanti, C. Mauro, G. Wang, A.S. Nair, H. Fu, S. Angeletti, S. Spoto, M. Fogolari, F. Romano, D. Aksentijevic, W. Liu, B. Li, L. Cheng, L. Jiang, J. Vuononvirta, T.R. Poobalasingam, D.M. Smith, M. Ciccozzi, E. Solito, F. M. Marelli-Berg, Preservation of microvascular barrier function requires CD31 receptor-induced metabolic reprogramming, Nat. Commun. 11 (1) (2020) 3595.
[65] E. Mrak, F. Guidobono, G. Moro, G. Fraschini, A. Rubinacci, I. Villa, Calcitonin gene-related peptide (CGRP) inhibits apoptosis in human osteoblasts by β-catenin stabilization, J. Cell. Physiol. 225 (3) (2010) 701–708.